Resolution modeling in PET imaging: Theory, practice, benefits, and pitfalls

Arman Rahmim[a)]
Departments of Radiology, and Electrical and Computer Engineering, Johns Hopkins University, Baltimore, Maryland 21287

Jinyi Qi
Department of Biomedical Engineering, University of California, Davis, California 95616

Vesna Sossi
Department of Physics & Astronomy, University of British Columbia, Vancouver, British Columbia V6T 1Z1, Canada

(Received 7 December 2012; revised 22 February 2013; accepted for publication 26 March 2013; published 6 May 2013)

In this paper, the authors review the field of resolution modeling in positron emission tomography (PET) image reconstruction, also referred to as point-spread-function modeling. The review includes theoretical analysis of the resolution modeling framework as well as an overview of various approaches in the literature. It also discusses potential advantages gained via this approach, as discussed with reference to various metrics and tasks, including lesion detection observer studies. Furthermore, attention is paid to issues arising from this approach including the pervasive problem of edge artifacts, as well as explanation and potential remedies for this phenomenon. Furthermore, the authors emphasize limitations encountered in the context of quantitative PET imaging, wherein increased intervoxel correlations due to resolution modeling can lead to significant loss of precision (reproducibility) for small regions of interest, which can be a considerable pitfall depending on the task of interest.
 [http://dx.doi.org/10.1118/1.4800806]

Key words: PET, image reconstruction, resolution modeling, PSF modeling

I. INTRODUCTION

Positron emission tomography (PET) is a powerful molecular imaging modality enabling measurements of radiotracer distributions *in vivo*. At the same time, PET imaging continues to be affected by a number of resolution degrading factors,[1] which translate to undesired cross-contamination between adjacent functional regions with distinct activities, referred to as the partial volume effect (PVE).[2]

This issue has been tackled via a number of postreconstruction partial volume correction (PVC) methods.[3] These methods can be broadly grouped into (i) region-of-interest (ROI)-based and (ii) voxel-based techniques. The first set of methods (e.g., Refs. 4–9) produces improved estimates to mean ROI uptake, utilizing anatomical information as commonly extracted from segmented MRI images, but they commonly involve assumptions of PET tracer distribution homogeneity within the anatomical regions, and importantly, do not produce *images*. Voxel-based methods, by contrast, do produce images. Examples include partition-based[10–13] or multiresolution[14–16] methods, though these techniques typically include simplifying assumptions. Iterative deconvolution[17] is another possibility, but can lead to enhanced noise levels (though promising enhancements involving regularization[18] or denoising[19] have been noted).

An alternative approach to PVC (that also reduces image noise) has been to incorporate anatomical information within the PET image *reconstruction* task[20] (from MRI or CT images, e.g., as are readily available and fairly reliably coaligned in dual-modality PET/CT imaging[21,22] and increasingly so with emerging PET/MRI imaging[23–25]). This anatomy-guided reconstruction approach is commonly achieved via Bayesian maximum *a posteriori* (MAP) reconstruction, incorporating segmented anatomical images, in which intervoxel intensity variations are penalized within the regions, while allowing for large intervoxel variations across the boundaries (e.g., Refs. 26 and 27). Such utilization of anatomical knowledge has been demonstrated by theory and simulations to be superior to postprocessing techniques.[28] In fact, anatomy guided PET reconstruction allows concurrent improvements in both the effective spatial resolution and signal-to-noise ratios in the reconstructed images. Nonetheless, a number of simplifying assumptions are commonly made (e.g., uniformity in radiopharmaceutical uptake within anatomic labels): to this end, more sophisticated approaches[29–34] have been investigated, though they are often seen to introduce a number of additional parameters to be further fine-tuned for particular tasks of interest. This approach thus remains an open area of interest.

An altogether distinct approach to this problem, referred to as resolution (or point-spread-function; PSF) modeling, which this work reviews, aims to model the very phenomena that degrade resolution within the reconstruction algorithm. In particular, following the introduction of statistical image reconstruction methods in PET,[35,36] and the so-called system matrix, it has become possible to accurately model the relationship between the object and projection space.[37] The accuracy with which the system matrix is defined has a critical role in the quality of the reconstructed images, and as such, it is potentially promising to model and incorporate

various resolution degrading effects within the PET image reconstruction task. Besides subject motion, a number of physical processes degrade image resolution in PET: these include positron range, photon noncollinearity, and detector-related effects (including crystal widths, intercrystal scattering and intercrystal penetration). One may then aim to model and incorporate these processes within the system matrix of the statistical image reconstruction algorithm, as is commonly performed for normalization and attenuation correction,[38] and has also been proposed for scatter modeling[39,40] and motion compensation.[41–46]

In what follows, we provide some theoretical considerations for the concept of resolution modeling in Sec. II, which includes consideration of approaches to simplify resolution modeling (Sec. II.A), as well as comparison of cascaded vs unified reconstruction (e.g., conventional reconstruction followed by PVC vs comprehensive resolution modeling) (Sec. II.B). This will be followed by a discussion of the various resolution modeling strategies as invoked in the field (Sec. III), including detector response (Sec. III.A) and positron range modeling (Sec. III.B). Strengths and limitations of resolution modeling in various imaging contexts and tasks will be discussed in Sec. IV, including particular attention to performance evaluations using conventional metrics (Sec. IV.A) vs observer studies (Sec. IV.B), the issue of edge artifacts (Sec. IV.C), and considerations and reservations in quantitative imaging (Sec. IV.D). This will be followed by concluding remarks in Sec. V.

II. THEORETICAL CONSIDERATIONS

Let us denote the system matrix as $\mathbf{P} \in \mathbb{R}^{J\times I}$ whose elements p_{ij} model the probability that an event generated in voxel j ($j = 1\ldots J$) is detected along a line-of-response (LOR) i ($i = 1\ldots I$). The system matrix may be factorized into several components:[47,48]

$$\mathbf{P} = \mathbf{P}_{\text{det.sens}}\mathbf{P}_{\text{det.blur}}\mathbf{P}_{\text{attn}}\mathbf{P}_{\text{geom}}\mathbf{P}_{\text{positron}} \tag{1}$$

representing the sequential nature of the physical processes, where the image-space component $\mathbf{P}_{\text{positron}} \in \mathbb{R}^{J\times J}$ models blurring effect in the image space, such as positron range, $\mathbf{P}_{\text{geom}} \in \mathbb{R}^{I\times J}$ models the geometrical mapping from the image space to the sinogram space that is determined by the solid angle subtended from each voxel to the faces of each detector pair, $\mathbf{P}_{\text{attn}} \in \mathbb{R}^{I\times I}$ is a diagonal matrix containing attenuation factors, $\mathbf{P}_{\text{det.blur}} \in \mathbb{R}^{I\times I}$ models detector blurring effects including crystal penetration, intercrystal scattering, and crystal misidentification, and $\mathbf{P}_{\text{det.sens}} \in \mathbb{R}^{I\times I}$ is a diagonal detector normalization matrix. Strictly speaking, $\mathbf{P}_{\text{det.blur}}\mathbf{P}_{\text{attn}}\mathbf{P}_{\text{geom}}$ are not factorizable because photon attenuation and detector blurring effects depend on the specific path that a photon travels within each LOR. However, especially for modern scanners with small detector elements, the factored model is fairly accurate. Similarly, photon noncollinearity should be modeled in the geometric component $\mathbf{P}_{\text{geom}}$ of the system matrix; however, as an approximation to simplify the system matrix computation, one can assume photon noncollinearity is depth-independent and model it in the detector blurring matrix $\mathbf{P}_{\text{det.blur}}$.

Overall, approaches to resolution modeling vary in terms of how they approximate the above formulation and how the individual resolution degrading terms are estimated. The majority of these techniques focus on estimation of $\mathbf{P}_{\text{det.blur}}$ which we discuss in Sec. III.A, while positron range modeling methods (that can be especially important for isotopes producing high energy positrons) are discussed in Sec. III.B.

II.A. Model simplifications: projection-space vs. image-space resolution modeling

Ignoring the diagonal matrices for normalization and attenuation, the factored system matrix is often further simplified to a product of two matrices. In one case, the blurring effect is modeled in the sinogram space with $\mathbf{P} = \mathbf{BG}$, while in the other case, the blurring is modeled in the image space with $\mathbf{P} = \mathbf{GR}$. In both cases, $\mathbf{G}$ can be a simple line integral model. $\mathbf{B}$ and $\mathbf{R}$ denote the sinogram and image domain blurring matrices, respectively.

Both simplified models have been used in practice, as we will review in Sec. III. When the positron range effect is negligible, such as PET imaging with ^{18}F tracers, the sinogram blurring model ($\mathbf{BG}$) is adequate. In addition, as a consequence of the central slice theorem, space-invariant positron range blurring (which, in the Fourier domain, is multiplicative) can be modeled in the sinogram space via a radial filter. Thus, the sinogram blurring model can be used in many situations without loss of modeling accuracy. One limitation is that it cannot model a space-variant positron range effect. By comparison, the image domain PSF model ($\mathbf{GR}$) is capable of modeling space-variant blurring caused by positron range. It can also model some detector blurring effects. However, the accuracy of the model depends on the overlap of the range spaces (also called column space) of matrices $\mathbf{P}$ and $\mathbf{G}$.[49] When the range space of $\mathbf{P}$ is inside the range space of $\mathbf{G}$, an image domain blurring matrix $\mathbf{R}$ can be found to model all detector blurring effects.

Often, matrix $\mathbf{R}$ is obtained by reconstructing a set of point source measurements. When the point source data are of high counting statistics, the matrix $\mathbf{R}$ can then be approximated via the least squares (LS) solution arriving at $\mathbf{R} = (\mathbf{G}^{\mathrm{T}}\mathbf{G})^{-1}\mathbf{G}^{\mathrm{T}}\mathbf{P}$. It then follows, as we show below, that *even* when the range condition is not satisfied, the LS reconstruction of any object $\mathbf{x}$ (with projection data $\mathbf{y} = \mathbf{Px}$) using the $\mathbf{GR}$ model is unbiased, so long as $\mathbf{G}^{\mathrm{T}}\mathbf{P}$ and $\mathbf{G}^{\mathrm{T}}\mathbf{G}$ are both invertible:

$$\begin{aligned}\hat{\mathbf{x}} &= (\mathbf{R}^{\mathrm{T}}\mathbf{G}^{\mathrm{T}}\mathbf{GR})^{-1}\mathbf{R}^{\mathrm{T}}\mathbf{G}^{\mathrm{T}}\mathbf{y} = \mathbf{R}^{-1}(\mathbf{G}^{\mathrm{T}}\mathbf{G})^{-1}(\mathbf{R}^{\mathrm{T}})^{-1}\mathbf{R}^{\mathrm{T}}\mathbf{G}^{\mathrm{T}}\mathbf{Px}\\ &= \mathbf{R}^{-1}(\mathbf{G}^{\mathrm{T}}\mathbf{G})^{-1}\mathbf{G}^{\mathrm{T}}\mathbf{Px} = \mathbf{R}^{-1}\mathbf{Rx} = \mathbf{x}\end{aligned} \tag{2}$$

However, the noise of the LS reconstruction is

$$\begin{aligned}\boldsymbol{\Sigma}_{\hat{\mathbf{x}}} &= (\mathbf{R}^{\mathrm{T}}\mathbf{G}^{\mathrm{T}}\mathbf{GR})^{-1}\mathbf{R}^{\mathrm{T}}\mathbf{G}^{\mathrm{T}}\boldsymbol{\Sigma}_{\mathbf{y}}\mathbf{GR}(\mathbf{R}^{\mathrm{T}}\mathbf{G}^{\mathrm{T}}\mathbf{GR})^{-1}\\ &= \mathbf{R}^{-1}(\mathbf{G}^{\mathrm{T}}\mathbf{G})^{-1}\mathbf{G}^{\mathrm{T}}\boldsymbol{\Sigma}_{\mathbf{y}}\mathbf{G}(\mathbf{G}^{\mathrm{T}}\mathbf{G})^{-1}(\mathbf{R}^{\mathrm{T}})^{-1}\\ &= (\mathbf{G}^{\mathrm{T}}\mathbf{P})^{-1}\mathbf{G}^{\mathrm{T}}\boldsymbol{\Sigma}_{\mathbf{y}}\mathbf{G}(\mathbf{P}^{\mathrm{T}}\mathbf{G})^{-1}\end{aligned}$$

For white noise, i.e., $\boldsymbol{\Sigma}_y = \sigma^2 \boldsymbol{I}$, the above equation reduces to

$$\boldsymbol{\Sigma}_{\hat{\mathbf{x}}} = \sigma^2 [\mathbf{P}^{\mathrm{T}} \mathbf{G} (\mathbf{G}^{\mathrm{T}} \mathbf{G})^{-1} \mathbf{G}^{\mathrm{T}} \mathbf{P}]^{-1}. \quad (3)$$

Under the same condition, the covariance of the reconstruction obtained using the true system matrix $\mathbf{P}$ is

$$\boldsymbol{\Sigma}_{\mathbf{0}} = \sigma^2 [\mathbf{P}^{\mathrm{T}} \mathbf{P}]^{-1}.$$

Now let $\mathbf{A} = \mathbf{G}(\mathbf{G}^{\mathrm{T}}\mathbf{G})^{-1}\mathbf{G}^{\mathrm{T}}$, noting that it is an orthogonal projection onto the range of $\mathbf{G}$ [The term *orthogonal projection* here is in the context of linear algebra: a matrix $\mathbf{A}$ is an orthogonal projection if $\mathbf{A}^2 = \mathbf{A}$ and $\mathbf{A}^{\mathrm{T}} = \mathbf{A}$.]. It is then easy to see that for any vector $\mathbf{t} \in R^J$, we have

$$\langle \mathbf{APt}, \mathbf{APt} \rangle = \mathbf{t}^{\mathrm{T}} \mathbf{P}^{\mathrm{T}} \mathbf{APt} = \langle \mathbf{Pt}, \mathbf{APt} \rangle .$$

Combined with the Cauchy inequality, it then follows that $\langle \mathbf{APt}, \mathbf{APt} \rangle = \sqrt{\langle \mathbf{Pt}, \mathbf{Pt} \rangle \langle \mathbf{APt}, \mathbf{APt} \rangle}$ and therefore $\langle \mathbf{APt}, \mathbf{APt} \rangle \leq \langle \mathbf{Pt}, \mathbf{Pt} \rangle$; thus $\mathbf{t}^{\mathrm{T}} \mathbf{P}^{\mathrm{T}} \mathbf{G} (\mathbf{G}^{\mathrm{T}} \mathbf{G})^{-1} \mathbf{G}^{\mathrm{T}} \mathbf{Pt} \leq \mathbf{t}^{\mathrm{T}} \mathbf{P}^{\mathrm{T}} \mathbf{Pt}$. As such, $\mathbf{P}^{\mathrm{T}}\mathbf{P} - \mathbf{P}^{\mathrm{T}}\mathbf{G}(\mathbf{G}^{\mathrm{T}}\mathbf{G})^{-1}\mathbf{G}^{\mathrm{T}}\mathbf{P}$ is a positive semidefinite matrix. Consequently, $[\mathbf{P}^{\mathrm{T}}\mathbf{G}(\mathbf{G}^{\mathrm{T}}\mathbf{G})^{-1}\mathbf{G}^{\mathrm{T}}\mathbf{P}]^{-1} - [\mathbf{P}^{\mathrm{T}}\mathbf{P}]^{-1}$ is also positive semidefinite (Corollary 7.7.4 in Ref. 50) and we have

$$\mathbf{t}^{\mathrm{T}} [\mathbf{P}^{\mathrm{T}} \mathbf{G} (\mathbf{G}^{\mathrm{T}} \mathbf{G})^{-1} \mathbf{G}^{\mathrm{T}} \mathbf{P}]^{-1} \mathbf{t} \geq \mathbf{t}^{\mathrm{T}} [\mathbf{P}^{\mathrm{T}} \mathbf{P}]^{-1} \mathbf{t}. \quad (4)$$

Let $\mathbf{t}$ be the indicator function for an ROI. The left-hand and right-hand sides of Eq. (4) are the variances of the estimated total ROI activity from the **GR** model and the true system model $\mathbf{P}$, respectively. Thus, Eq. (4) shows that for ROI quantification, the variance from the **GR** model is greater than or equal to that from the true system model. As a special case, when the ROI contains a single pixel, Eq. (4) indicates that the pixel variance of the GR model is greater than or equal to that of the true system model.

The above analysis shows that the **GR** model can result in an unbiased estimate but with higher variance. Therefore, one cannot evaluate the accuracy of a system model solely based on noise-free reconstructions (or equivalently, spatial resolution measurements). Noise property of the reconstruction should be examined. One example to illustrate this noise amplification is to consider $\mathbf{P}$ as the system matrix for an ideal fully 3D PET and $\mathbf{G}$ as the system matrix for the corresponding 2D PET that consists of the direct planes only. Obviously the range spaces of $\mathbf{P}$ and $\mathbf{G}$ do not overlap and the range condition is not satisfied. When the **BG** model is used, the matrix $\mathbf{B}$ can be set to perform inverse Fourier rebinning[51] thus $\mathbf{P} = \mathbf{BG}$. When the **GR** model is used, we have $\mathbf{R} = \mathbf{I}$ because the fully 3D PET and 2D PET both contain the same spatial blurring model. However, reconstructions using the **GR** model (2D PET) result in much higher noise than when the **BG** model (3D PET) is utilized.

II.B. Unified vs cascaded modeling of resolution degradation

When a factored system matrix is used, the PET system can be considered as a cascade of a set of subsystems. For image reconstruction, one can choose either a sequential approach by performing normalization correction, attenuation correction, sinogram deblurring, inverse radon transform, and image deconvolution, step-by-step, or a single inversion of the whole system matrix. When all the matrices in Eq. (1) are invertible, the two approaches are equivalent (the ML solution is the analytic inverse). However, the invertibility of the geometric projection matrix is rarely true, because $\mathbf{P}_{\mathrm{geom}}$ is often a tall matrix, especially for fully 3D PET and TOF scanners. Therefore, when using the sequential approach, one has to model the noise propagation carefully. Otherwise, the benefit of noise modeling of an iterative reconstruction can be lost. This is because while noise in the raw PET data can be well modeled by independent Poisson distribution, noise properties become complex after preprocessing steps.[52] For this reason, most sinogram restoration methods, such as those by Huesman *et al.*[52] and Liang,[53] are combined with an analytic image reconstruction method. This approach may pose computational advantages, but can result in noise amplification.

When the image domain blurring matrix $\mathbf{R}$ is invertible, one can perform ML image reconstruction with $\mathbf{G}$ followed by image deconvolution using $\mathbf{R}$ to obtain the same result as that obtained by using **GR** in an iterative image reconstruction, assuming both algorithms are iterated to convergence. This is because a function of the ML estimate is the ML estimate of the function,[54] and thus, if $\mathbf{z}$ is an ML estimate of $\mathbf{Rx}$ (i.e., when only modeling $\mathbf{G}$), then $\mathbf{R^{-1}z}$ is an ML estimate of $\mathbf{x}$ (i.e., modeling **GR**). However, intermediate iterates of the two algorithms can be very different because they highly depend on the algorithms and the initial images. In fact, the sequential approach involving EM reconstruction using $\mathbf{G}$ followed by image deconvolution using $\mathbf{R}$, which can be thought of as performing postreconstruction PVC, was found in a study to result in slightly higher noise relative to single unified reconstruction.[55] The performances became similar after inserting an image smoothing step within the sequential approach in order to reduce noise.

It is worth noting that though theoretically appealing, inclusion of all components in the forward- and backprojection operations does not necessary result in faster convergence for image reconstruction. In fact, it has been shown that with resolution modeling, the initial convergence speed, as measured by contrast recovery vs iteration, can be slower than that without a resolution model.[56,57] In particular, when the condition numbers of the matrices on the right hand side of Eq. (1) are very different, decoupling them may result in faster convergence.[58,59] One approach to decoupling the matrices without affecting the image quality is to use the nested EM algorithm.[58] Although the approach was proposed for direct reconstruction of linear parametric images from dynamic PET data, the method is applicable to PET image reconstruction with a factored system matrix. With this method, each image update using the **GR** model can be implemented by one iteration of EM reconstruction using $\mathbf{G}$ followed by multiple iterations of image deconvolution using $\mathbf{R}$.[59] The advantages of this method would be that it gives the same solution as using the **GR** model directly and it does not require the matrices to be invertible. However, the individual elements of matrices $\mathbf{G}$ and $\mathbf{R}$ should be nonnegative for the EM algorithm to be applicable.

III. RESOLUTION MODELING STRATEGIES

The majority of resolution modeling approaches focus on estimation and incorporation of $\mathbf{P}_{\text{det.blur}}$ which we discuss next (Sec. III.A). Some of these methods also inherently incorporate positron range modeling, e.g., when performing characterization using ^{18}F (e.g., Refs. 60 and 61) or ^{22}Na (e.g., Refs. 49 and 62) sources (which have very similar positron range properties to one another[63]). Nonetheless, Sec. III.B discussed methods specifically aimed at positron range modeling, which is of particular interest for imaging tasks involving more energetic positrons, e.g., ^{82}Rb PET, wherein resulting positron range contributions can compete significantly[64] with other resolution degrading factors.

III.A. Detector response modeling

We first note that 3D PET projection data are described via four coordinates, an example of which is (r, θ, z, ϕ) denoting the radial bin, azimuthal angle, axial bin, and axial angle, respectively, while there are three coordinates, Cartesion (x, y, z), that define the image space. As such, there has been a preference to perform resolution modeling in the image space, as described next.

III.A.1. Image-space modeling

Specifically, Reader *et al.*[65,66] modeled resolution blurring entirely with an image-space component $\mathbf{P}_{\text{reso}} \in \mathbb{R}^{J\times J}$ of the system matrix:

$$\mathbf{P} = \mathbf{P}_{\text{det.sens}}\mathbf{P}_{\text{attn}}\mathbf{P}_{\text{geom}}\mathbf{P}_{\text{reso}}, \tag{5}$$

where $\mathbf{P}_{\text{reso}}$ was modeled incorporating Gaussian fits to the PSF (as obtained from preliminary reconstructions without resolution modeling). The approach is very straightforward to implement, does not pose a significant computational burden, is feasible for list-mode image reconstructions, and produces images of high quality. Nonetheless, the PSF is in practice not purely Gaussian. Sureau *et al.*[60] used a similar shift-invariant approach, though using sum of two Gaussians to better model the shape of the PSF, followed by assessment of impact on dynamic PET studies and estimated kinetic parameters. Antich *et al.*[55] also used a shift-invariant approach in small animal imaging, though utilizing a generalized convolution kernel involving summation of a Gaussian and two non-Gaussian terms.

The abovementioned overall approach, however, did not model the presence of varying intercrystal blurring that is known to lead to the parallax effect, the degradation of resolution as one moves away from the center of the field-of-view (FOV). Further generalizations by (i) Rahmim *et al.*,[67] (ii) Rapisarda *et al.*,[62] (iii) Cloquet *et al.*,[49] and (iv) Kotasidis *et al.*[61] used space-varying blurring kernels [as estimated from (i)–(iii) regular line or point sources or (iv) simultaneously printed[68,69] point sources]. This included additional inclusion of (i)–(v) anisotropicity, (ii)–(iii) asymmetry, and (iii)–(iv) non-Gaussianity to better model the PSF. Overall, these more generalized approaches demonstrated some improvements in resolution, and in contrast vs noise tradeoff curves.

III.A.2. Projection-space modeling

The abovementioned image-based methods, however, can only be considered as approximations relative to the appropriate projection-space modeling of $\mathbf{P}_{\text{det.blur}}$ (see theoretical analysis in Sec. II). In its most general form, $\mathbf{P}_{\text{det.blur}}$, combined with the projection operation $\mathbf{P}_{\text{geom}}$, equates a seven-dimensional[70] system response function (SRF) $S(r, \theta, z, \phi; x_0, y_0, z_0)$, mapping a given voxel (x_0, y_0, z_0) to (r, θ, z, ϕ). (Factoring out the projection operation $\mathbf{P}_{\text{geom}}$, and using an eight-dimensional SRF $S(r, \theta, z, \phi; r_0, \theta_0, z_0, \phi_0)$, that maps given projection coordinates $(r_0, \theta_0, z_0, \phi_0)$ to their blurred counterparts (r, θ, z, ϕ), is actually less general: this is because depth-information (distance of source-voxel to detector) is lost, which may be important in the presence of axial mashing (spanning).[71,72]) In practice, the use of such functions is not feasible computationally and/or storage-wise, and as a result, reduced dimensionality has been sought by various projection-space approaches in the literature: these methods can be categorized into those based on (a) analytic models, (b) Monte Carlo (MC) simulations, and (c) measured datasets, which we elaborate next.

(a) *Analytic models:* Lecomte *et al.*[73] and a number of subsequent works,[74–78] involving further refinements, applications, and comparisons used an analytic model of intercrystal penetration determined by the angle of incidence. This was followed by an analytic model of radial blurring in the *coincidence* aperture function; i.e., to extend individual detector blurring to that of radial blurring for detector pairs in coincidence. The SRF as such was effectively reduced to a two-dimensional $S(r; r_0)$, given the 2D PET context in above formulations and the fact that in cylindrical scanners the angle of incidence is purely determined by the radial bin r_0 of the incident ray. This approach, however, neglected contributions due to intercrystal *scattering*, and only incorporated intercrystal penetration.

Rahmim *et al.*[79] extended the approach by convolving the response by a shift-invariant 2D Gaussian kernel $S_{\text{scatter}}(r, z)$ of intercrystal scattering, which was assumed to be independent of the angle of incidence, unlike the penetration kernel, and was estimated via measured projection data of a point source at the center of the FOV. The response was also convolved by a 2D Gaussian kernel $S_{\text{non–colin.}}(r, z; r_0)$ which modeled photon noncollinearity via a 2D Gaussian with FWHM $= 0.0022\ L$, which only depended on separation of the detector pairs L, itself also determined by the radial bin r_0 for cylindrical scanners. Above works, however, were primarily developed in the context of 2D PET acquisition. In the context of 3D PET, Huesman *et al.*[80] developed an analytic formulation for intercrystal penetration using a multiray tracing method. The same approach was refined by Moehrs *et al.*[81] to include the intercrystal scattering effect.

(b) *MC simulations:* Mumcuoglu *et al.*[82] and Qi *et al.*[47,48] used MC simulations to estimate the SRF, which included photon noncollinearity, intercrystal penetration, and

intercrystal scattering, and applied this technique to different animal and human-PET scanners. The approach effectively simplified the SRF to a three-dimensional $S(r, \theta; r_0)$ estimating blurring only among the radial and azimuthal components within any given direct or oblique 2D sinograms, with the blurring function purely determined by the incident radial bin r_0, attributed to azimuthal angular symmetry. By contrast, Alessio *et al.*[70] performed MC simulations to estimate a simplified SRF $S(r, z; r_0)$ that performed blurring along the radial and axial bins. The latter was performed in the context of Fourier-rebinning[83] followed by 2D PET reconstructions.

(c) *Measured datasets:* To accurately quantify the SRF, ideal experiments would employ elaborate *collimated* point sources. Otherwise, it is not straightforward to distinguish contributions from the various neighboring coordinates. An alternative approach is to use statistical methods to separate these various contributions when utilizing noncollimated points sources, as proposed in Ref. 56 in the case of 2D PET to quantify blurring along both radial and azimuthal directions. Most approaches, however, as described next, utilize noncollimated point and/or line source measurements in conjunction with more simplified SRF models, dropping characterization of blurring along the azimuthal angle θ (and the axial angle ϕ in 3D PET).

In particular, Panin *et al.*, in the context of 2D PET (Ref. 71) and 3D PET,[72] used a 3D positioning robot to perform very elaborate point source measurements, involving 1599 individual positions, for a whole-body PET/CT scanner. The SRF, as modeled along the radial r and axial z directions, was a function of the radial bin r_0, axial bin z_0, and axial angle ϕ_0 of the incident LOR (and additionally the depth d of the source voxel along the LOR in the case of axial blurring, due to the complicating presence of axial mashing). This work was incorporated within the HD-PET release by Siemens in a number of clinical PET/CT scanners, and subsequently studied in a number of applications, e.g., cardiac imaging.[84,85]

The previously mentioned model $S(r, z; r_0)$ by Alessio *et al.*[70] actually showed minimal improvements relative to a further simplified model $S(r; r_0)$ performing blurring only along the radial direction, which was subsequently adopted in a later work:[63] the approach involved measurement of projection-space profiles for point sources scanned at 14 radial positions across the transaxial FOV: profiles for intermediate radial positions were estimated via linear interpolations of discrete cosine transform (DCT) coefficients from the measured profiles. The resulting $S(r; r_0)$ is depicted in Fig. 1. This approach, with minor modifications, was adopted by GE within the released SharpIR algorithm.

A similar model was previously pursued by Frese *et al.*[86] though for an entirely different geometry of two opposing detector banks (with adjustable separation), and quantified using a line source scanned across the FOV in very small steps of $\Delta r_0 = 0.5$ mm. Lee *et al.*[87] also used a similar model $S(r; r_0)$, performing line source measurements at 14 radial positions r_0 whose individual profiles were fitted using six-parameter asymmetrical Gaussian–Lorentzian curves, and individually interpolated across the spectrum of r_0 values.

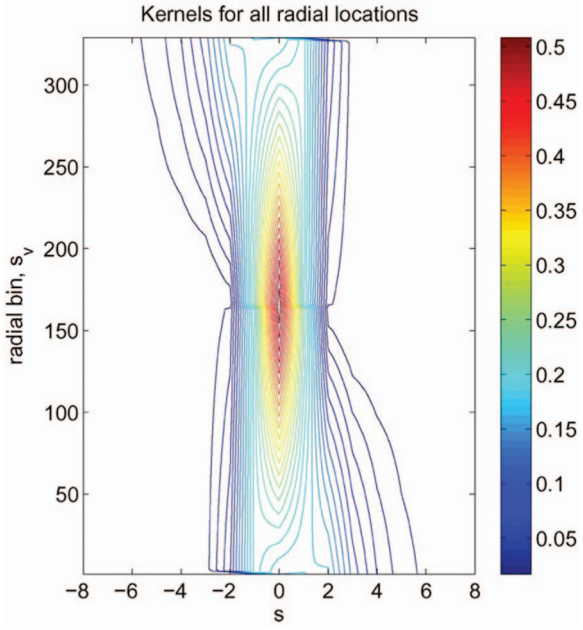

FIG. 1. Isocontour plot of radial blurring kernels (shown along the x axis) interpolated for all incident radial bins r_0 (y axis). Reprinted with permission from A. M. Alessio, C. W. Stearns, T. Shan, S. G. Ross, S. Kohlmyer, A. Ganin, and P. E. Kinahan, IEEE Trans. Med. Imaging **29**(3), 938–949 (2010). Copyright © 2010 by IEEE.

Recently Zhou and Qi[88] used combined image-space and projection-space modeling to improve the model accuracy. The blurring matrices were estimated from point source data using a maximum likelihood approach. The advantage of the combined approach is that one can use a very simple geometric projection matrix to reduce reconstruction time without any noticeable degradation in the image quality.

III.B. Positron range modeling

The abovementioned system matrix formulation (1) allows modeling of the positron range effect within the reconstruction algorithm. As PET imaging is primarily performed with ^{18}F or ^{11}C labeled tracers, which depict relatively small positron ranges compared to other resolution degrading effects, most abovementioned works either do not model the positron range, or use ^{18}F or ^{22}Na sources, which depict very similar positron range properties to one another,[63] to inherently incorporate impact of positron range.

Here we discuss methods specifically aimed at positron range modeling for imaging tasks involving more energetic positrons, e.g., ^{82}Rb PET, wherein resulting positron range contributions can compete significantly[64] with other resolution degrading factors.

Ruangma *et al.*[89] performed positron range modeling for three positron emitting isotopes of Cu, namely, Cu-60, Cu-61, Cu-64, assuming a uniform medium (e.g., soft tissue or water). To simulate the propagation of positrons in matter, the software package EGS4+PRESTA (Electron Gamma Shower Code Version 4+ Parameter Reduced Electron Step Transport Algorithm)[90] was utilized.

By contrast, Rahmim *et al.*[79] applied an analytic model of positron range to ^{82}Rb PET image reconstruction. They achieved this in reference to the seminal work of Palmer and Brownell[91] wherein an analytic model of positron range was developed and shown to closely agree with experimental[92] as well as simulated[93] results. Specifically, for a given emitted positron energy E, the annihilation density $D(\mathbf{r},E)$ was modeled as a 3D symmetric Gaussian with its standard deviation being a function of the density d, effective atomic weight A_{eff} and atomic number Z_{eff} of the medium. The overall distribution was then evaluated as

$$\bar{D}(\mathbf{r}) = \int D(\mathbf{r}, E)N(E)dE, \tag{6}$$

where $N(E)$ is the positron emission energy probability density, and for which an analytic model has also been implemented.[79,94,95] The resulting overall distribution was then fit via a 3D biexponential model, and used within the EM reconstruction framework.

III.B.1. Space-variant modeling

It is natural to consider the fact that positron range distributions within media of different properties (density, effective atomic weight/number) such as lung, soft tissue, and bone can be very different (heterogeneity), which also can result in anisotropicity of positron distributions near the boundaries of different media. It is also imaginable that modeling and incorporation of such differences could lead to further improvements in image qualities and imaging tasks.

Bai *et al.*[96] proposed an approach wherein multiple convolutions were performed, initially for a given positron start position, and subsequently to surviving positrons in their potentially different local medium, attempting to model medium inhomogeneity as positrons propagate. The authors showed visual enhancements, for Cu-60 and Cu-64 imaging, compared to the case of no modeling at all (see discussion later).

In the context of ^{82}Rb modeling, Rahmim *et al.*[97] computed the overall annihilation distribution for a number of materials in the human body, including interpolations for material properties in-between. A nearly exponential function was then used to fit the annihilation distributions, followed by relating the resulting function parameters to attenuation coefficients μ (at 511 keV) which can be estimated from accompanying CT scans (as routinely done for attenuation correction). The authors then used an incremental step update approach to model anisotropicity of positron distributions near the boundaries, followed by incorporation within the system matrix of the EM algorithm.

Alessio *et al.*[98] proposed an alternative framework, based on a formula fit to empirical beta decay data by Katz and Penfold[99] to compute 1D positron annihilation distributions for a range of densities, and the corresponding attenuation coefficients μ. A biexponential function was fit to the distributions, and its parameters were plotted as a function of μ. 3D annihilation distributions were then generated by normalizing the 1D distributions with the surface area of the sphere at each radius. To adjust for variations across boundaries, the parameters for the originating voxel and particular voxel of interest were averaged. The authors subsequently incorporated this model within the forward-projection step of the EM algorithm. It is worth noting that this latter reconstruction approach, where the forward- and backprojection steps are not matched, has the potential to exhibit divergent results (e.g., see Ref. 44).

In contrast to abovementioned approximating methods, MC simulation is the ideal technique to estimate positron propagations for diverse anatomies and radioactive profiles, and yet iterative (on-the-fly) estimation and incorporation of such modeling within the reconstruction task is computationally very expensive. Fu and Qi[100] proposed a novel approximate error correction formulation, wherein image reconstructions were performed using less accurate (yet more feasible) system matrix modeling, but a *data precompensation* step involving extensive MC simulations was implemented to correct for the mismatch between the "true" system matrix vs the approximate one used. However, the authors showed that a single data precorrection step was not sufficient, and that at least every few iterations, a new MC simulation had to be performed.

Overall, it remains an open question as to how important it is to perform space-variant modeling of positron range. All abovementioned works performed comparisons primarily with respect to no resolution modeling. Bai *et al.* acknowledged in a later publication[101] that their approach only "revealed little improvement over the infinite homogenous model," though they found this likely attributed to the lack of anisotropic propagation modeling within each stage of their convolutional model. In any case, in the context of ^{82}Rb myocardial perfusion, though myocardium-to-lung contrast vs noise performance was observed[97] to be enhanced with respect to space-invariant modeling, it does not follow that defect detection can be necessarily enhanced, given the fact that the heart is primarily surrounded, within positron range distances, by blood and tissue all of which have nearly identical materials properties. Alternative potential exploration of this approach within noncardiac ^{82}Rb imaging[102] and other imaging applications remains to be thoroughly evaluated.

IV. STRENGTHS AND LIMITATIONS

Resolution modeling commonly leads to visually enhanced images, depicting higher contrast for small or narrow structures[126] (e.g., see Fig. 2). Nonetheless, it is important to carefully quantify various quantitative metrics, and to properly assess potentially improved performance for various tasks and applications, which we review next.

IV.A. Resolution, contrast, and noise

Resolution modeling methods, as discussed in Sec. III, are very commonly seen to lead to improved resolution (e.g., see Fig. 3), which translates to enhanced contrast recovery for extended objects. At the same time, it is critical to note that resolution modeling can significantly modify the noise structure. (Noise here indicates the statistical uncertainty

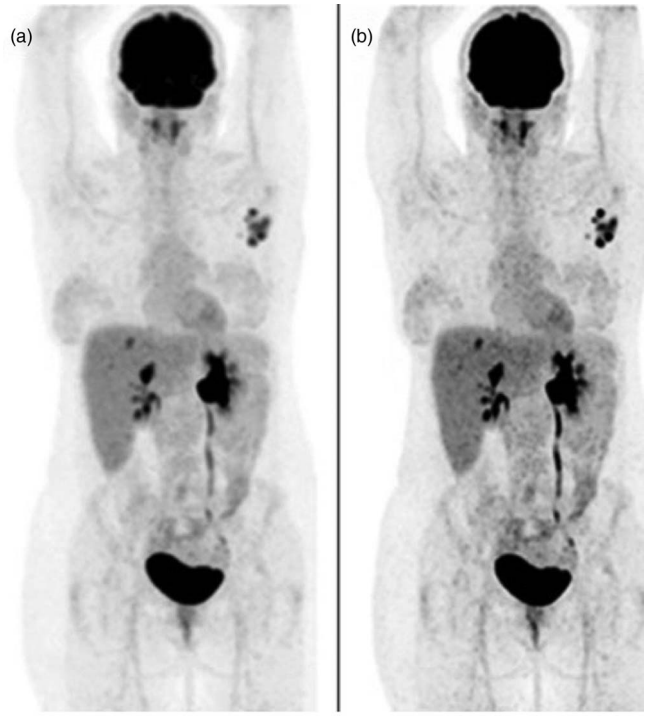

FIG. 2. PET/CT scan in the staging of left breast cancer. Detection performed 1 h after the IV infusion of 185 MBq of 18F-FDG. Iterative reconstruction (a) without and (b) with resolution modeling (using the commercial SharpIR software from GE Healthcare, itself closely based on Ref. 63). Enhanced visualization of the lymph nodes has been achieved. Reprinted with permission from A. Pecking, D. Bellet, and J. Alberini, Clin. Exp. Metastasis **29**, 847–852 (2012). Copyright © 2012 by Springer Publishing.

arising from the random nature of radioactive emissions, which could include various associated photon emissions (e.g., cascade gamma rays), though in practice, resolution modeling efforts have been primarily limited to "clean" radionuclides.) In particular, resolution modeling can lead to (i) diminished voxel variance while (ii) increasing intervoxel covariance, as demonstrated in Ref. 103 utilizing a noise propagation model[104] in iterative reconstruction, or in Ref. 60 using experimental multiple-noise-realization measurements.

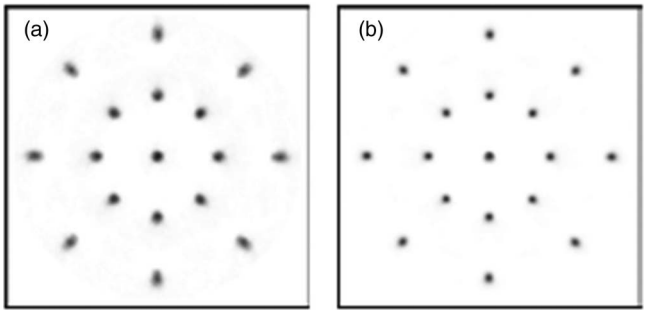

FIG. 3. Transverse sections of point source images reconstructed with FORE+OSEM: (a) without and (b) with resolution modeling. Reprinted with permission from K. Lee, P. E. Kinahan, J. A. Fessler, R. S. Miyaoka, M. Janes, and T. K. Lewellen, Phys. Med. Biol. **49**(19), 4563–4578 (2004). The particular resolution modeling approach used in the reference was described in Sec. III.A under projection-space modeling methods). Copyright © 2004 by Springer.

The latter is what gives rise to the "lumpiness" of the noise texture from resolution modeling.

Tong *et al.*[105] provided formulations for how varying variance and covariance are expected to impact various measures of noise, as we discuss next. For a uniform region r consisting of N voxels with voxel variance σ_0^2 for each voxel and intervoxel covariance $\mathrm{cov}_{i,j}$ between any two voxels i and j, let us consider two different measures of noise: (i) spatial variance, a measure of image roughness, calculated for a given noise realization, across voxel values f_i within the region-of-interest (ROI) with mean m:

$$\sigma^2_{\text{spatial}} = \frac{1}{N-1}\sum_{i=1}^{N}(f_i - m)^2. \tag{7}$$

(ii) Variance of ROI mean uptake m_r, across multiple noise realizations $r = 1 \ldots R$, with mean overall uptake $\bar{m}$:

$$\sigma^2_{\text{ensemble}} = \frac{1}{R-1}\sum_{r=1}^{R}(m_r - \bar{m})^2. \tag{8}$$

The expectations of these statistics can be shown to be given by

$$\begin{aligned} E\left[\sigma^2_{\text{spatial}}\right] &= \sigma_0^2 - \frac{1}{(N-1)N}\sum_{i\neq j}\mathrm{cov}_{i,j} \\ &= \sigma_0^2 - \frac{2}{(N-1)N}\sum_{i>j}\mathrm{cov}_{i,j} \end{aligned} \tag{9}$$

$$\begin{aligned} E\left[\sigma^2_{\text{ensemble}}\right] &= \frac{\sigma_0^2}{N} + \frac{1}{N^2}\sum_{i\neq j}\mathrm{cov}_{i,j} \\ &= \frac{\sigma_0^2}{N} + \frac{2}{N^2}\sum_{i>j}\mathrm{cov}_{i,j} \end{aligned} \tag{10}$$

Two observations can be made: (i) diminished voxel variance σ_0^2 and increased covariance $\mathrm{cov}_{i,j}$ translate to a reduced measures of *spatial* noise or image roughness,[103,105] while they work against one another for ensemble variance of mean ROI values: the latter is because positive covariances contribute positively to ensemble noise.[105] In fact, (ii) covariance contributions are greater in the case of ensemble noise because the first term includes normalization of σ_0^2 by N, which enhances relative contributions of the second term. As such, noise, when measured spatially, can be significantly reduced due to resolution modeling, for a given iteration number, contrary to the ensemble measure of noise which could actually not change[105] or even increase[106] This issue of increased variability, i.e., degradation of precision in quantitative studies, is elaborated in Sec. IV.D, including an illustrated example. Overall, however, dual-metric contrast (or resolution) vs noise tradeoff curves (often generated using increasing reconstruction iterations) are commonly reported to depict enhanced performance whether noise is defined as σ_{spatial} (e.g., Refs. 49, 61, 62, 66, 79, and 84) or σ_{ensemble} (e.g., Refs. 49, 60, 63, and 70), but plots in the latter category tend to depict less significant improvements, consistent with abovementioned analytic observations. We suggest in Sec. IV.B that a more thorough analysis of the noise structure, e.g., through

the noise power spectrum, may be needed to arrive at a more thorough analysis of the impact of resolution modeling.

IV.B. Observer studies

Dual-metric tradeoff curve analysis can potentially serve as a good initial step to quantitatively compare different techniques.[107,108] As such, they can be appropriately used to narrow down the range of reconstruction parameters to be subsequently studied in observer studies, which are then used to confirm or modify the preliminary findings of preferring one tradeoff curve to another, and to determine the optimal point (e.g., iteration number) within a specific tradeoff curve.

Furthermore, it is worth noting that the abovementioned noise metrics may disregard valuable information. To see this, for simplicity, let us first assume a system with shift-invariant resolution and stationary noise. Consider the modulation transfer function (MTF) which is the Fourier transform of the PSF, normalized by the area (volume) A of the PSF (A should ideally be $\sim$1 with proper calibration, but may not be especially in the case of non-linear reconstruction algorithms). We also define the noise power spectrum (NPS) as the Fourier transform of the noise covariance. For a detection task involving a difference signal $\Delta f(\mathbf{r})$, such as a lesion to be detected, the inter-class (lesion absent vs. present) signal-to-noise (SNR) is given by (e.g. see Ref. 109):

$$SNR^2 = A^2 \int d^q k \, |\Delta F(\mathbf{k})|^2 \frac{MTF^2(\mathbf{k})}{NPS(\mathbf{k})} = A^2 \int d^q f \, |\Delta F(\mathbf{k})|^2 \, NEQ(\mathbf{k}) \tag{11}$$

where q is the dimension of the image and $\Delta F(\mathbf{k})$ is the Fourier transform of the difference signal. The above expression can be arrived at assuming an ideal observer with signal- and background-known-exactly (SKE/BKE) having (a) Gaussian noise or (b) Poisson noise in the weak-signal limit, or (c) in the case of the linear Hotelling observer (Eqs. 13.238, 13.239, 13.256 of Ref. 54, respectively). The ratio $MTF^2(\mathbf{k})$ to $NPS(\mathbf{k})$ referred to as the noise-equivalent quanta (NEQ) can be thought of as a "window" through which the observer "sees", and thus the NEQ quantifies how much of the frequency content is transmitted through the imaging and reconstruction. We also note that under assumption of normality of the observer metric, which is the case for a linear observer under Gaussian noise, the area-under-curve (AUC) in ROC analysis is directly related to the SNR according to[54]

$$\mathrm{AUC} = \frac{1}{2} + \frac{1}{2}\mathrm{erf}\left(\frac{\mathrm{SNR}}{2}\right), \tag{12}$$

where $\mathrm{erf}(z)$ is the error function defined by $\mathrm{erf}(z) = \frac{2}{\sqrt{\pi}} \int_0^z \mathrm{d}y \exp[-y^2]$.

One thus notes that a detection task is not fully determined by simplified noise metrics; rather a more thorough description of intervoxel correlations, such as the NPS, can provide a more comprehensive picture. Next, we note that one can imagine the widened intervoxel covariance structure due to resolution modeling to lead to narrower NPS; e.g., by analogy to the Fourier transform of a Gaussian distribution. As such one could conjecture that the NEQ, already enhanced by wider MTF due to better recovery of higher frequencies, will be further boosted, at higher frequencies, due to division by diminished NPS values. This was reported in a dissertation[110] in the case of collimator-detector response function (CDRF) compensation[111] in SPECT imaging, and recently[127] in the case of resolution modeling in PET: in fact complex NPS structures were observed, including *increased* mid-frequency components of the NPS and diminished high-frequency components, relative to no compensation, ultimately demonstrating limited NEQ improvements. Overall, the abovementioned framework, coupled with the complex nature of the NPS and thus NEQ, may hold a key to explaining why in the inclusion of resolution modeling, observer task performance may result in relatively less improvements compared to those observed in conventional resolution/contrast vs noise analysis.

In the context of resolution modeled PET imaging, Kadrmas *et al.*[112,113] performed elaborate tumor detection evaluation studies using a sophisticated whole-body phantom composed of multiple individual phantoms with realistic FDG uptake levels, and including numerous "shell-less" ^{68}Ge silicone gel lesions. The studies included application of numeric channelized nonprewhitened; CNPW (Ref. 114) as well as human observers. The results, in the context of localization ROC (LROC) analysis, indicated significant improvement upon inclusion of resolution modeling. Figure 4 shows the impact of resolution modeling in the second study, which revealed additional significant improvements due to further inclusion of time-of-flight (TOF) acquisition capability. Similar relative patterns were observed by Schaefferkoetter *et al.*[115] in ROC/LROC analysis of numeric (CNPW, and channelized Hotelling observer; CHO) as well as human observer studies involving addition of separately scanned small spheres to the lung or the liver in clinical patient scans. However, when resolution modeling was utilized without the aid of TOF, improvements were limited to lung lesions, and liver lesions exhibited no improvements. Interestingly, retrospective analysis of clinical FDG PET/CT studies by Akamatsu *et al.*[116] (though evaluating liver SNRs, not lesion detectability) also revealed significant improvements when including TOF capability, and more so when combining TOF and resolution modeling, but not when resolution modeling only was employed. Finally, a recent simulation-based numeric (CHO) observer study of myocardial perfusion (MP) also revealed non-enhanced MP defect detectability performance upon inclusion of resolution modeling.[127]

IV.C. Edge artifacts

Resolution modeling can lead to notable edge artifacts, reminiscent of the Gibbs ringing overshoot at the edges. (As a function including a discontinuity (e.g., step function) is represented using a Fourier series with finite number of terms, an overshoot is observed at the point of discontinuity. This overshoot is also accompanied by ringing. Overall, this effect is referred to as the Gibbs phenomenon and is related to the sinc

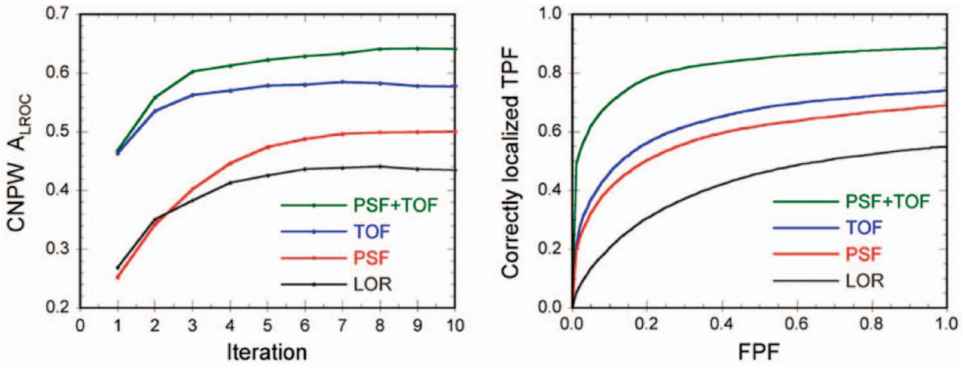

FIG. 4. Results for (left) model observer study and (right) human observer study, providing comparison and ranking of four reconstruction algorithms, namely, standard OSEM reconstruction (LOR), coupled with resolution modeling (PSF), with TOF, or with both (PSF+TOF). Model observer results plot area under LROC curve versus number of iterations. Human observer LROC curves demonstrate distinctions in performance for the four algorithms, and confirm model observer results. Reprinted with permission from D. J. Kadrmas, M. E. Casey, M. Conti, B. W. Jakoby, C. Lois, and D. W. Townsend, J. Nucl. Med. **50**(8), 1315–1323 (2009). Copyright © 2009 by Society of Nuclear Medicine and Molecular Imaging (SNMMI).

function which is the impulse response of a perfect low-pass filter.) An example is shown in Fig. 5 involving reconstructions of a clinical FDG scan. With increasingly small regions, this effect can manifest itself in the form of a visible dip at the center (due to enhanced edges), and with sufficiently small ROIs, where the edge artifacts begin to merge, this can lead to overshoots;[106,117] both effects are seen in Fig. 6. This issue also challenges accuracy in quantifications of small uptake regions, as elaborated in Sec. IV.D.

Edge artifacts were recognized early on (even in reconstructions without formal resolution modeling): in particular Synder *et al.*[118] attributed this to two phenomenon: (1) mismatch between the true projection kernel and the kernel used in the reconstruction; (2) contamination of the high frequency

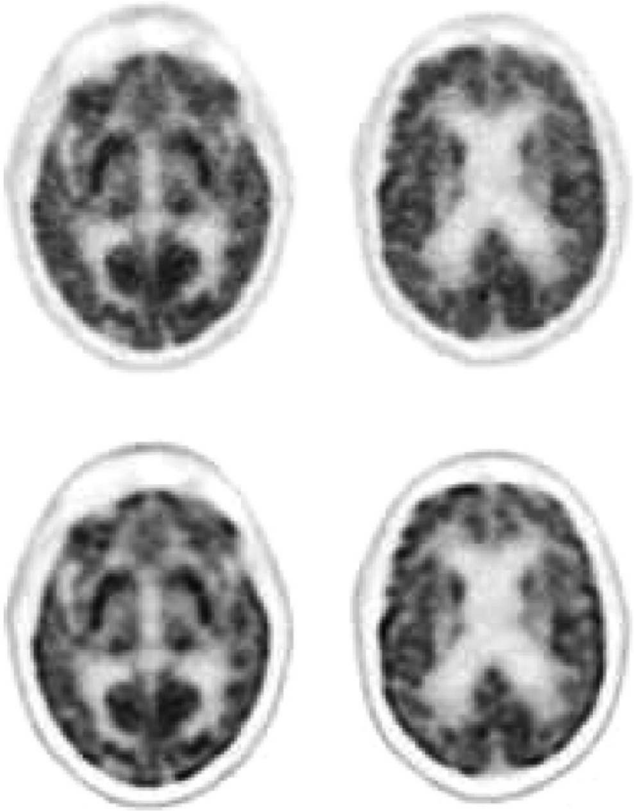

FIG. 5. Two transaxial slices from OSEM+3 mm postfilter (top), and OSEM+PSF modeling (bottom) for a clinical FDG scan. Images have matched color scales and matched pixel-to-pixel variability in central white matter. Reprinted with permission from A. M. Alessio, C. W. Stearns, T. Shan, S. G. Ross, S. Kohlmyer, A. Ganin, and P. E. Kinahan, IEEE Trans. Med. Imaging **29**(3), 938–949 (2010). Copyright © 2010 by IEEE.

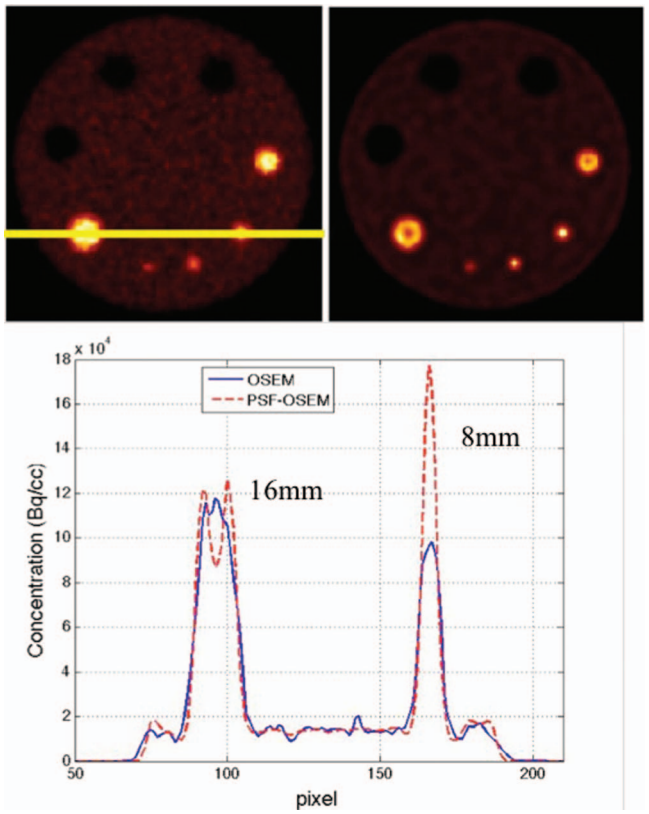

FIG. 6. OSEM reconstructed images of a phantom obtained without and with resolution (PSF) modeling, and profile through the center of 16 and 8 mm cylindrical insets. Inset-to-background concentration ratio was 8:1. From Bai and Esser, *Nuclear Science Symposium Conference Record (NSS/MIC)*, pp. 2263–2266, 2010. Copyright © 2010 by IEEE. Reprinted by permission of IEEE.

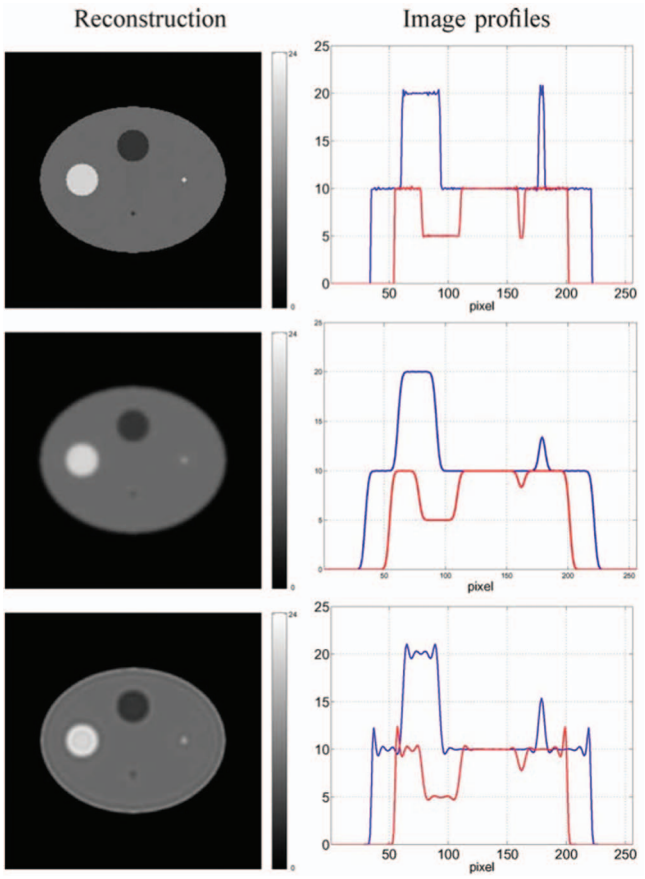

FIG. 7. Reconstructed images at iteration 500 for three different scenarios. Top to bottom: no data blurring/no-PSF recon, 14 mm data blurring/no-PSF recon, 14 mm data blurring/14 mm PSF recon. Left to right: reconstructed images, and horizontal and vertical profiles through center of the phantom. Reprinted with permission from S. Tong, A. M. Alessio, K. Thielemans, C. Stearns, S. Ross, and P. E. Kinahan, IEEE Trans. Nucl. Sci. **58**(5), 2264–2275 (2011). Copyright © 2011 by IEEE.

components of the true kernel (which fall very rapidly towards zero) due to noise contributions including those from machine precision: the high frequencies, needed to reconstruct regions near sharp transition, thus cannot be appropriately recovered within the deconvolution approach. However, in a very illustrative simulation, Tong *et al.*[119] simplified the imaging problem to an idealized scenario only involving image-space blurring (no projections and no noise), and applied the EM algorithm to recover the original image, demonstrating continued presence of edge artifacts (Fig. 7). The authors then attempted to explain the problem from a system theory perspective, quantifying the rank and condition number, i.e., the largest singular value divided by the smallest, of the blurring kernels for different kernel sizes, demonstrating increasing rank deficiency and conditions numbers with increased blurring.

Proposed solutions to the edge artifact problem include:

(1) An approach is to use a reconstruction filter that underestimates the true PSF. This approach, originally referred as the resolution kernel method,[118,120] was framed as a reconstruction algorithm that estimated a desired blurred version of the object, and not the object itself, thus utilizing underestimated resolution widths. The approach is very effective at suppressing edge artifacts (e.g., see Refs. 106 and 119). (This algorithm is distinct from the method of sieves also pursued by Snyder *et al.*:[120,121] the method of sieves seeks to constrain the EM solution to a bandwidth limited subspace of all possible solutions, and turns out to be equivalent to using the standard EM algorithm with the additional usage of an image-space blur component K, followed by convolution of the final estimated image with the blurring kernel K. However, this approach can only reduce noise but not edge artifacts.) Watson[122] proposed an explanation for this, and a derivation for the required amount of underestimation. He suggested that direct use of measured PSF values within reconstruction actually overestimated the PSF because reconstructions include additional "numerical" mechanisms of point spread, primarily due to image discretization and the projection operations. Using the heuristic assumption that modeled PSF widths and numerical PSF widths combined quadratically (Gaussian convolutions), Watson proposed a first order approximation to estimate the "numerical" blur and subsequently the amount by which modeled PSF had to be underestimated with respect to the measured PSF.
Nonetheless, we note that this cannot entirely explain the observed edge artifacts, because in a number of works the "true" PSF actually had the exact same[66,119] structure as the modeled PSF, and thus numerical blur was applied not at all or equally to both, an example of which is shown in Fig. 8: in particular, slight

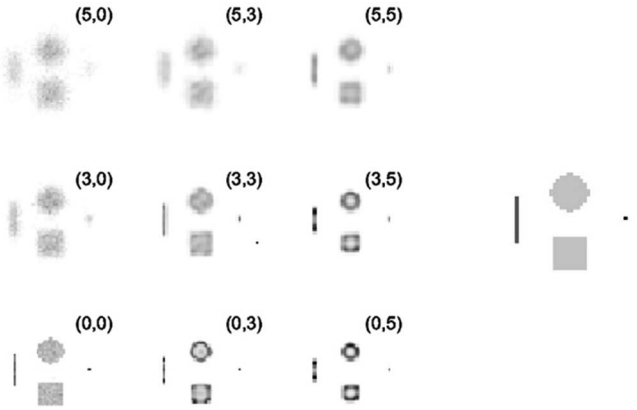

FIG. 8. Reconstructions (of the true image; shown on the right) for varying true PSF kernel FWHM (first number in brackets) and for varying system-model convolution kernel FWHM (second number). The leftmost column corresponds to reconstructing without system resolution modeling (*, 0), for different levels of acquisition blurring. If resolution is overmodeled (by using a convolution kernel too large), artifacts appear. Matching the convolution kernel size with the resolution of the acquisition process, in which case the diagonal lines of images from the bottom left corner to the top right corner are obtained, results in visually improved images; however Gibbs artifacts can still occur [e.g., (5.5)]. Reprinted with permission from A. J. Reader, P. J. Julyan, H. Williams, D. L. Hastings, and J. Zweit, IEEE Trans. Nucl. Sci. **50**(5), 1392–1397 (2003). Copyright © 2003 by IEEE.

edge artifacts are still seen on the top-right image. These observations can be easily reproduced in simple EM recovery of blurred images, e.g., as performed by Tong *et al.*,[119] where edge artifacts are commonly obtained. This issue needs to be better understood theoretically. Blurred versions of images with edge artifacts look very similar to blurred versions of the true images, and our simulations show that log-likelihood values are nearly identical. It appears that the EM algorithm approaches the ML solution by gradually recovering the high-frequency content because high-frequency information is attenuated by the $1/\omega_r$ response of the backprojection operation in the update equation. This is actually the underlying mechanism whereby the EM reconstruction can be regularized by early stopping of the iterations to avoid high-frequency noise. However, the lack of high-frequency content can cause ringing artifacts near sharp boundaries, similar to the Gibbs ringing artifacts in truncated Fourier series. Moreover, in some cases, the convergence of a high-frequency component can be nonmonotonic and certain high-frequencies can even be amplified before convergence, which can further exaggerate the edge artifacts as shown by Tong *et al.*[119] Further research could shed light on alternative formulations that may better recover the high frequency content. In any case, Watson's approach would minimize the edge artifacts because it avoids overestimations of the PSF which is known to lead to even larger artifacts (e.g., middle-right image in Fig. 8).

(2) Performing object-specific modulation transfer analysis, Tong *et al.*[119] demonstrated an amplified frequency band in the Fourier domain, corresponding to ringing artifacts at the edges, which was shown to be stable for phantoms of different sizes and contrast levels. Subsequently, they proposed a band suppression filter, to mitigate the edge artifacts, demonstrating enhanced resolution performance relative to a simple low-pass filter.

IV.D. Quantitative studies

Quantification accuracy includes the effects of variance as well as bias. Both need to be ideally minimized, but in practice there is often a tradeoff, and the particular task determines the importance of each factor. As discussed in Sec. IV.A, increased intervoxel correlations can result in: (i) improved contrast recovery due to reduced partial volume effect, and also (ii) reduced spatial roughness, but unchanged or even increased variability, thus reduced reproducibility, if the ROI size is comparable to the correlations lengths (lumpiness of structure). This effect is of particular relevance in a situation where the biological outcome of interest is derived from

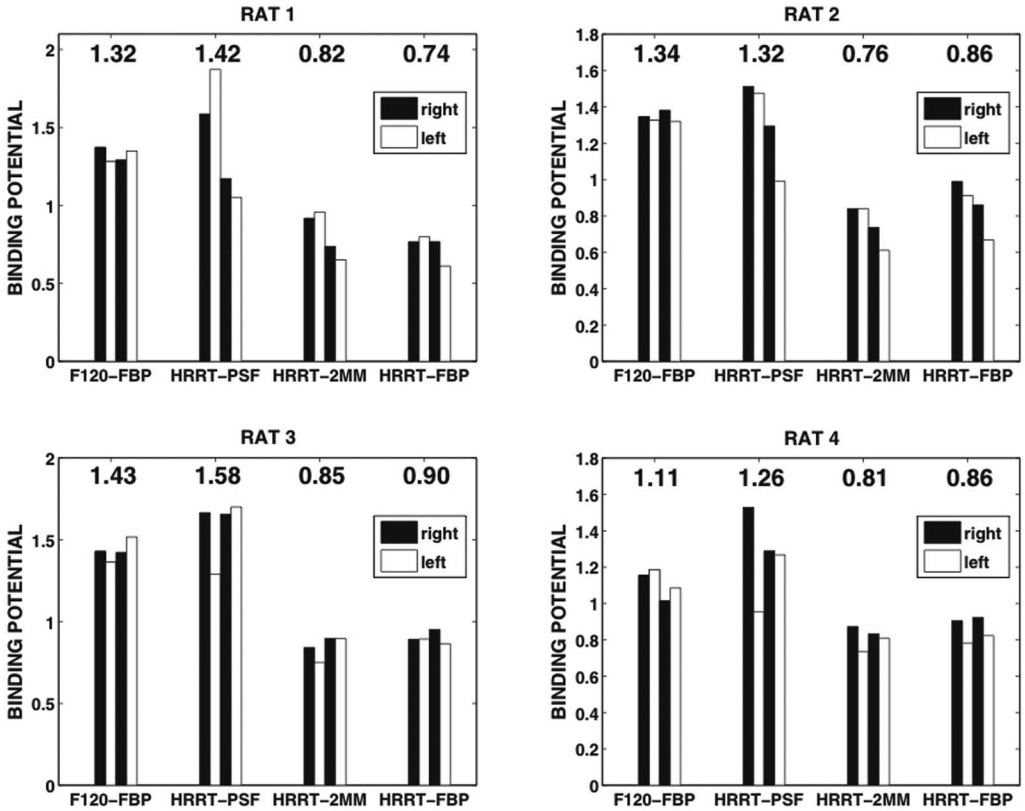

FIG. 9. Binding potential values in the right (black) and left (white) striatum for each rat and each reconstruction type: F120-filtered backprojection, HRRT-filtered backprojection, HRRT-OSEM-OP followed by 2 mm smoothing, and HRRT-OSEM-OP with resolution modeling. The 4 bars in each group correspond to the four BP_{ND} (each animal was imaged twice on each scanner) values extracted from each scan of each rat on each camera. Reprinted with permission from S. A. Blinder, K. Dinelle, and V. Sossi, Med. Phys. **39**(8), 5073–5083 (2012). Copyright © 2012 by American Association of Physicists in Medicine (AAPM).

a quantitative comparison of radioactivity concentrations between different regions. This is the case, for example, when estimating tissue input binding potentials BP_{ND}.[123]

At first glance it might appear tempting to take advantage of the increased effective resolution offered by resolution modeling algorithms to improve the quantification accuracy of the radioactivity concentration estimates in smaller structures and thus BP_{ND}. To this extent, Blinder *et al.*[106] compared BP_{ND} estimates of a dopaminergic tracer in a group of healthy rats imaged twice with the dedicated microPET Siemens Focus 120,[124] (considered as reference), with those obtained in identical scanning conditions on the high resolution research tomograph (HRRT). Data acquired on the latter scanner were reconstructed with and without resolution modeling. When resolution modeling is used the HRRT effective resolution [$\sim(1.8\ \text{mm})^3$; $(2.3)^3$ mm otherwise] becomes comparable to that of the Focus 120 [$\sim(1.7\ \text{mm})^3$]. The structure of relevance was the rat striata $(\sim 3.5\ \text{mm})^3$, composed by symmetrical right and left sides. As depicted in Fig. 9, the reconstruction of the HRRT data performed without resolution modeling led to a variability of 17%, and ~25% lower BP_{ND} values compared to those obtained from the Focus 120. By comparison, the magnitude of the BP_{ND} estimates was found to be better matched with the Focus 120 (but actually on average 7% higher) when the data were acquired on the HRRT and reconstructed with resolution modeling. The BP_{ND} estimate variability, in this case, was much higher for the HRRT, 26.8% compared to 5.9% obtained with the Focus 120. Interestingly, when individual BP_{ND} values were plotted (not shown here) as a function of the number of reconstruction iterations, a very different convergence pattern was observed between two virtually identical structures (left and right striatum) when resolution modeling was included in the reconstruction, partially explaining the large variability observed in Fig. 9.

Taken together these data show that while resolution modeling is effective at reducing the larger bias due to the partial volume effect, it does so at the expense of significantly increased variability and the introduction of a smaller bias due to edge artifacts. These results thus convey the important message that in a situation when the object size is commensurate with the width of the resolution kernel, resolution modeling must be used with caution as it can significantly decreases the reproducibility of the data. Its use may remain beneficial when partial volume induced bias, rather than noise, is the dominant problem. An example of this is when the blood input function is estimated from the images wherein resolution modeling can substantially improve the performance;[125] otherwise biased input function estimates can lead to erroneous results in kinetic parameter estimation, though, again, this will result in increased variability in the parameter estimates.

V. CONCLUSIONS

This paper presents an extensive review of the status of resolution modeling algorithms. Considerable effort has been devoted to this topic resulting in the development of a variety of approaches both for characterization of resolution degrading effects and for the correction of the resulting blurring during data reconstruction. Resolution modeling has resulted in significant improvements in image resolution and contrast, while the effect on noise, and the ultimate impact on signal detection, is less straightforward, which this review have attempted to shed more light on. It is also very important to notice that there are unresolved aspects, such as the presence of edge artifacts, which remain to be fully understood. Furthermore, while resolution modeling can produce images with reduced roughness, it can simultaneously lead to increased variability when quantification in small structures is required, which can pose a serious burden in quantitative studies. With the present status of knowledge, it is thus important to carefully assess in which conditions the use of resolution modeling is beneficial and warranted.

ACKNOWLEDGMENTS

The authors wish to acknowledge helpful discussions with, and presentations by, Dr. Adam Alessio and Dr. Benjamin Tsui in a continuing education (CE) session entitled "Resolution Modeling in Nuclear Medicine Imaging" at the Annual Society of Nuclear Medicine (SNM) Meeting, Miami, 2012. They also acknowledge helpful discussions with Dr. Shan Tong and Dr. Eric Frey. Partial support was provided by NIH Grant Nos. R01 EB000194 and RC4 EB012836.

[a]Author to whom correspondence should be addressed. Electronic mail: arahmim1@jhmi.edu

[1]A. Rahmim and H. Zaidi, "PET versus SPECT: Strengths, limitations and challenges," Nucl. Med. Commun. **29**(3), 193–207 (2008).
[2]M. Soret, S. L. Bacharach, and I. Buvat, "Partial-volume effect in PET tumor imaging," J. Nucl. Med. **48**(6), 932–945 (2007).
[3]O. G. Rousset, A. Rahmim, A. Alavi, and H. Zaidi, "Partial volume correction strategies in PET," PET Clin. **2**, 235–249 (2007).
[4]J. C. Mazziotta, M. E. Phelps, D. Plummer, and D. E. Kuhl, "Quantitation in positron emission computed tomography: 5. Physical-anatomical effects," J. Comput. Assist. Tomogr. **5**(5), 734–743 (1981).
[5]R. M. Kessler, J. R. Ellis, and M. Eden, "Analysis of emission tomographic scan data: Limitations imposed by resolution and background," J. Comput. Assist. Tomogr. **8**(3), 514–522 (1984).
[6]O. G. Rousset, Y. Ma, and A. C. Evans, "Correction for partial volume effects in PET: Principle and validation," J. Nucl. Med. **39**(5), 904–911 (1998).
[7]Y. Du, B. M. W. Tsui, and E. C. Frey, "Partial volume effect compensation for quantitative brain SPECT imaging," IEEE Trans. Med. Imaging **24**(8), 969–976 (2005).
[8]C. Labbe, J. C. Froment, A. Kennedy, J. Ashburner, and L. Cinotti, "Positron emission tomography metabolic data corrected for cortical atrophy using magnetic resonance imaging," Alzheimer Dis. Assoc. Disord. **10**(3), 141–170 (1996).
[9]J. A. Aston, V. J. Cunningham, M. C. Asselin, A. Hammers, A. C. Evans, and R. N. Gunn, "Positron emission tomography partial volume correction: Estimation and algorithms," J. Cereb. Blood Flow Metab. **22**(8), 1019–1034 (2002).
[10]T. O. Videen, J. S. Perlmutter, M. A. Mintun, and M. E. Raichle, "Regional correction of positron emission tomography data for the effects of cerebral atrophy," J. Cereb. Blood Flow Metab. **8**(5), 662–670 (1988).
[11]H. W. Muller-Gartner, J. M. Links, J. L. Prince, R. N. Bryan, E. McVeigh, J. P. Leal, C. Davatzikos, and J. J. Frost, "Measurement of radiotracer concentration in brain gray matter using positron emission tomography: MRI-based correction for partial volume effects," J. Cereb. Blood Flow Metab. **12**(4), 571–583 (1992).
[12]O. G. Rousset, Y. Ma, D. F. Wong, and A. C. Evans, in *Quantitative Functional Imaging with Positron Emission Tomography*, edited by R. Carson,

M. E. Daube-Witherspoon, and P. Herscovitch (Academic, San Diego, 1998), Vol. 1, pp. 67–75.
[13]C. C. Meltzer, J. K. Zubieta, J. M. Links, P. Brakeman, M. J. Stumpf, and J. J. Frost, "MR-based correction of brain PET measurements for heterogeneous gray matter radioactivity distribution," J. Cereb. Blood Flow Metab. **16**(4), 650–658 (1996).
[14]A. Le Pogam, M. Hatt, P. Descourt, N. Boussion, C. Tsoumpas, F. E. Turkheimer, C. Prunier-Aesch, J. L. Baulieu, D. Guilloteau, and D. Visvikis, "Evaluation of a 3D local multiresolution algorithm for the correction of partial volume effects in positron emission tomography," Med. Phys. **38**(9), 4920–4933 (2011).
[15]M. Shidahara, C. Tsoumpas, A. Hammers, N. Boussion, D. Visvikis, T. Suhara, I. Kanno, and F. E. Turkheimer, "Functional and structural synergy for resolution recovery and partial volume correction in brain PET," Neuroimage **44**(2), 340–348 (2009).
[16]N. Boussion, M. Hatt, F. Lamare, Y. Bizais, A. Turzo, C. Cheze-Le Rest, and D. Visvikis, "A multiresolution image based approach for correction of partial volume effects in emission tomography," Phys. Med. Biol. **51**, 1857–1876 (2006).
[17]B. K. Teo, Y. Seo, S. L. Bacharach, J. A. Carrasquillo, S. K. Libutti, H. Shukla, B. H. Hasegawa, R. A. Hawkins, and B. L. Franc, "Partial-volume correction in PET: Validation of an iterative postreconstruction method with phantom and patient data," J. Nucl. Med. **48**(5), 802–810 (2007).
[18]A. S. Kirov, J. Z. Piao, and C. R. Schmidtlein, "Partial volume effect correction in PET using regularized iterative deconvolution with variance control based on local topology," Phys. Med. Biol. **53**(10), 2577–2591 (2008).
[19]N. Boussion, C. C. Le Rest, M. Hatt, and D. Visvikis, "Incorporation of wavelet-based denoising in iterative deconvolution for partial volume correction in whole-body PET imaging," Anglais **36**(7), 1064–1075 (2009).
[20]B. Bai, Q. Z. Li, and R. M. Leahy, "Magnetic resonance-guided positron emission tomography image reconstruction," Semin. Nucl. Med. **43**(1), 30–44 (2013).
[21]D. W. Townsend, "Dual-modality imaging: Combining anatomy and function," J. Nucl. Med. **49**(6), 938–955 (2008).
[22]O. Mawlawi and D. W. Townsend, "Multimodality imaging: An update on PET/CT technology," Anglais **36**, 15–29 (2009).
[23]G. Delso, S. Furst, B. Jakoby, R. Ladebeck, C. Ganter, S. G. Nekolla, M. Schwaiger, and S. I. Ziegler, "Performance measurements of the Siemens mMR integrated whole-body PET/MR scanner," J. Nucl. Med. **52**(12), 1914–1922 (2011).
[24]M. D. Seemann, "Whole-body PET/MRI: The future in oncological imaging," Technol. Cancer Res. Treat. **4**(5), 577–582 (2005).
[25]H. F. Wehrl, A. W. Sauter, M. S. Judenhofer, and B. J. Pichler, "Combined PET/MR imaging—Technology and applications," Technol. Cancer Res. Treat. **9**(1), 5–20 (2010).
[26]B. Lipinski, H. Herzog, E. Rota Kops, W. Oberschelp, and H. W. Muller-Gartner, "Expectation maximization reconstruction of positron emission tomography images using anatomical magnetic resonance information," IEEE Trans. Med. Imaging **16**(2), 129–136 (1997).
[27]C. Comtat, P. E. Kinahan, J. A. Fessler, T. Beyer, D. W. Townsend, M. Defrise, and C. Michel, "Clinically feasible reconstruction of 3D whole-body PET/CT data using blurred anatomical labels," Phys. Med. Biol. **47**(1), 1–20 (2002).
[28]J. Nuyts, K. Baete, D. Beque, and P. Dupont, "Comparison between MAP and postprocessed ML for image reconstruction in emission tomography when anatomical knowledge is available," IEEE Trans. Med. Imaging **24**(5), 667–675 (2005).
[29]J. E. Bowsher, V. E. Johnson, T. G. Turkington, R. J. Jaszczak, C. R. Floyd, and R. E. Coleman, "Bayesian reconstruction and use of anatomical a priori information for emission tomography," IEEE Trans. Med. Imaging **15**(5), 673–686 (1996).
[30]A. Rangajaran, I.-T. Hsiao, and G. Gindi, "A Bayesian joint mixture framework for the integration of anatomical information in functional image reconstruction," J. Math Imaging Vis. **12**, 199–217 (2000).
[31]J. Nuyts, "The use of mutual information and joint entropy for anatomical priors in emission tomography," IEEE Nucl. Sci. Symp. Conf. Rec. **6**, 4149–4154 (2007).
[32]S. Somayajula, C. Panagiotou, A. Rangarajan, Q. Z. Li, S. R. Arridge, and R. M. Leahy, "PET image reconstruction using information theoretic anatomical priors," IEEE Trans. Med. Imaging **30**(3), 537–549 (2011).
[33]J. Tang and A. Rahmim, "Bayesian PET image reconstruction incorporating anato-functional joint entropy," Phys. Med. Biol. **54**, 7063–7075 (2009).
[34]J. Tang, H. Kuwabara, D. F. Wong, and A. Rahmim, "Direct 4D reconstruction of parametric images incorporating anato-functional joint entropy," Phys. Med. Biol. **55**(15), 4261 (2010).
[35]L. A. Shepp and Y. Vardi, "Maximum likelihood reconstruction for emission tomography," IEEE Trans. Med. Imaging **1**, 113–122 (1982).
[36]K. Lange and R. Carson, "EM reconstruction algorithms for emission and transmission tomography," J. Comput. Assist. Tomogr. **8**(2), 306–316 (1984).
[37]R. M. Leahy and J. Y. Qi, "Statistical approaches in quantitative positron emission tomography," Stat. Comput. **10**(2), 147–165 (2000).
[38]T. J. Hebert and R. Leahy, "Fast methods for including attenuation in the EM algorithm," IEEE Trans. Nucl. Sci. **37**(2), 754–758 (1990).
[39]R. Manavaki, A. J. Reader, C. Keller, J. Missimer, and R. J. Walledge, "Scatter modeling for 3-d PET list-mode EM reconstruction," in *Nuclear Science Symposium Conference Record, 2002* (IEEE, 2002), Vol. 1863, pp. 1863–1868.
[40]M. Tamal, A. J. Reader, P. J. Markiewicz, P. J. Julyan, and D. L. Hastings, "Noise properties of four strategies for incorporation of scatter and attenuation information in PET reconstruction using the EM-ML algorithm," IEEE Trans. Nucl. Sci. **53**(5), 2778–2786 (2006).
[41]J. Qi and R. H. Huesman, "List mode reconstruction for PET with motion compensation: A simulation study," in *Proceedings of IEEE International Symposium on Biomedical Imaging, Washington*, DC, USA, 7–10 July 2002 (2002), pp. 413–416.
[42]R. E. Carson, W. C. Barker, J.-S. Liow, and C. A. Johnson, "Design of a motion-compensation OSEM list-mode algorithm for resolution-recovery reconstruction for the HRRT," in *IEEE Nuclear Science Symposium Conference Record*, Portland, OR, USA, 19–25 October 2003 (2003), pp. 3281–3285.
[43]A. Rahmim, P. Bloomfield, S. Houle, M. Lenox, C. Michel, K. R. Buckley, T. J. Ruth, and V. Sossi, "Motion compensation in histogram-mode and list-mode EM reconstructions: Beyond the event-driven approach," IEEE Trans. Nucl. Sci. **51**, 2588–2596 (2004).
[44]A. Rahmim, J. C. Cheng, K. Dinelle, M. Shilov, W. P. Segars, O. G. Rousset, B. M. Tsui, D. F. Wong, and V. Sossi, "System matrix modelling of externally tracked motion," Nucl. Med. Commun. **29**(6), 574–581 (2008).
[45]A. Rahmim, K. Dinelle, J. C. Cheng, M. A. Shilov, W. P. Segars, S. C. Lidstone, S. Blinder, O. G. Rousset, H. Vajihollahi, B. M. Tsui, D. F. Wong, and V. Sossi, "Accurate event-driven motion compensation in high-resolution PET incorporating scattered and random events," IEEE Trans. Med. Imaging **27**(8), 1018–1033 (2008).
[46]J. Qi, "Calculation of the sensitivity image in list-mode reconstruction for PET," IEEE Trans. Nucl. Sci. **53**(5), 2746–2751 (2006).
[47]J. Qi, R. M. Leahy, S. R. Cherry, A. Chatziioannou, and T. H. Farquhar, "High-resolution 3D Bayesian image reconstruction using the microPET small-animal scanner," Phys. Med. Biol. **43**(4), 1001–1013 (1998).
[48]J. Qi, R. M. Leahy, H. Chinghan, T. H. Farquhar, and S. R. Cherry, "Fully 3D Bayesian image reconstruction for the ECAT EXACT HR+," IEEE Trans. Nucl. Sci. **45**(3), 1096–1103 (1998).
[49]C. Cloquet, F. C. Sureau, M. Defrise, G. Van Simaeys, N. Trotta, and S. Goldman, "Non-Gaussian space-variant resolution modelling for list-mode reconstruction," Phys. Med. Biol. **55**(17), 5045–5066 (2010).
[50]R. A. Horn and C. R. Johnson, *Matrix Analysis*, 2nd ed. (Cambridge University Press, Cambridge, UK, 2012).
[51]S. Cho, Q. Li, S. Ahn, B. Bai, and R. M. Leahy, "Iterative image reconstruction using inverse Fourier rebinning for fully 3-D PET," IEEE Trans. Med. Imaging **26**(5), 745–756 (2007).
[52]R. H. Huesman, E. M. Salmeron, and J. R. Baker, "Compensation for crystal penetration in high-resolution positron tomography," IEEE Trans. Nucl. Sci. **36**(1), 1100–1107 (1989).
[53]Z. G. Liang, "Detector response restoration in image-reconstruction of high-resolution positron emission tomography," IEEE Trans. Med. Imaging **13**(2), 314–321 (1994).
[54]H. Barrett and K. Myers, *Foundations of Image Science* (Wiley Interscience, 2004).
[55]P. Antich, R. Parkey, S. Seliounine, N. Slavine, E. Tsyganov, and A. Zinchenko, "Application of expectation maximization algorithms for image resolution improvement in a small animal PET system," IEEE Trans. Nucl. Sci. **52**(3), 684–690 (2005).

[56]M. S. Tohme and J. Qi, "Iterative image reconstruction for positron emission tomography based on a detector response function estimated from point source measurements," Phys. Med. Biol. **54**(12), 3709–3725 (2009).
[57]K. Thielemans, E. Asma, S. Ahn, R. M. Manjeshwar, T. Deller, S. G. Ross, C. W. Stearns, and A. Ganin, "Impact of PSF modelling on the convergence rate and edge behaviour of EM images in PET," in *Nuclear Science Symposium Conference Record (NSS/MIC), 2010* (IEEE, 2010), pp. 3267–3272.
[58]G. Wang and J. Qi, "Acceleration of the direct reconstruction of linear parametric images using nested algorithms," Phys. Med. Biol. **55**(5), 1505–1517 (2010).
[59]J. C. Matthews, G. I. Angelis, F. A. Kotasidis, P. J. Markiewicz, and A. J. Reader, "Direct reconstruction of parametric images using any spatiotemporal 4D image based model and maximum likelihood expectation maximisation," in *Nuclear Science Symposium Conference Record (NSS/MIC), 2010* (IEEE, 2010), pp. 2435–2441.
[60]F. C. Sureau, A. J. Reader, C. Comtat, C. Leroy, M.-J. Ribeiro, I. Buvat, and R. Trebossen, "Impact of image-space resolution modeling for studies with the high-resolution research tomograph," J. Nucl. Med. **49**(6), 1000–1008 (2008).
[61]F. A. Kotasidis, J. C. Matthews, G. I. Angelis, P. J. Noonan, A. Jackson, P. Price, W. R. Lionheart, and A. J. Reader, "Single scan parameterization of space-variant point spread functions in image space via a printed array: The impact for two PET/CT scanners," Phys. Med. Biol. **56**(10), 2917–2942 (2011).
[62]E. Rapisarda, V. Bettinardi, K. Thielemans, and M. C. Gilardi, "Image-based point spread function implementation in a fully 3D OSEM reconstruction algorithm for PET," Phys. Med. Biol. **55**(14), 4131–4151 (2010).
[63]A. M. Alessio, C. W. Stearns, T. Shan, S. G. Ross, S. Kohlmyer, A. Ganin, and P. E. Kinahan, "Application and evaluation of a measured spatially variant system model for PET image reconstruction," IEEE Trans. Med. Imaging **29**(3), 938–949 (2010).
[64]A. Rahmim, J. Tang, M. R. Ay, and F. Bengel, "4D respiratory motion-corrected Rb-82 myocardial perfusion PET imaging," IEEE Nucl. Sci. Symp. Conf. Rec. 3312–3316 (2010).
[65]A. J. Reader, S. Ally, F. Bakatselos, R. Manavaki, R. J. Walledge, A. P. Jeavons, P. J. Julyan, S. Zhao, D. L. Hastings, and J. Zweit, "One-pass list-mode EM algorithm for high-resolution 3-D PET image reconstruction into large arrays," IEEE Trans. Nucl. Sci. **49**(3), 693–699 (2002).
[66]A. J. Reader, P. J. Julyan, H. Williams, D. L. Hastings, and J. Zweit, "EM algorithm system modeling by image-space techniques for PET reconstruction," IEEE Trans. Nucl. Sci. **50**(5), 1392–1397 (2003).
[67]A. Rahmim, M. Lenox, C. Michel, A. J. Reader, and V. Sossi, "Space-variant and anisotropic resolution modeling in list-mode EM reconstruction," IEEE Nucl. Sci. Symp. Conf. Rec. **5**, 3074–3077 (2003).
[68]J. A. van Staden, H. du Raan, M. G. Loetter, A. van Aswegen, and C. P. Herbst, "Production of radioactive quality assurance phantoms using a standard inkjet printer," Phys. Med. Biol. **52**(15), N329–N337 (2007).
[69]V. Sossi, M. L. Camborde, G. Tropini, D. Newport, A. Rahmim, D. J. Doudet, and T. J. Ruth, "The influence of measurement uncertainties on the evaluation of the distribution volume ratio and binding potential in rat studies on a microPET R4: A phantom study," Phys. Med. Biol. **50**(12), 2859–2869 (2005).
[70]A. M. Alessio, P. E. Kinahan, and T. K. Lewellen, "Modeling and incorporation of system response functions in 3-D whole body PET," IEEE Trans. Med. Imaging **25**(7), 828–837 (2006).
[71]V. Y. Panin, F. Kehren, H. Rothfuss, D. Hu, C. Michel, and M. E. Casey, "PET reconstruction with system matrix derived from point source measurements," IEEE Trans. Nucl. Sci. **53**(1), 152–159 (2006).
[72]V. Y. Panin, F. Kehren, C. Michel, and M. Casey, "Fully 3-D PET reconstruction with system matrix derived from point source measurements," IEEE Trans. Med. Imaging **25**(7), 907–921 (2006).
[73]R. Lecomte, D. Schmitt, and G. Lamoureux, "Geometry study of a high resolution PET detection system using small detectors," IEEE Trans. Nucl. Sci. **31**(1), 556–561 (1984).
[74]D. Schmitt, B. Karuta, C. Carrier, and R. Lecomte, "Fast point spread function computation from aperture functions in high-resolution positron emission tomography," IEEE Trans. Med. Imaging **7**(1), 2–12 (1988).
[75]B. Karuta and R. Lecomte, "Effect of detector weighting functions on the point spread function of high-resolution pet tomographs—A simulation study," IEEE Trans. Med. Imaging **11**(3), 379–385 (1992).
[76]V. Selivanov, Y. Picard, J. Cadorette, S. Rodrigue, and R. Lecomte, "Detector response models for statistical iterative image reconstruction in high resolution PET," IEEE Trans. Nucl. Sci. **47**, 1168–1175 (2000).
[77]T. J. Holmes and D. C. Ficke, "Analysis of positron-emission tomography scintillation-detectors with wedge faces and inter-crystal septa," IEEE Trans. Nucl. Sci. **32**(1), 826–830 (1985).
[78]D. Strul, R. B. Slates, M. Dahlbom, S. R. Cherry, and P. K. Marsden, "An improved analytical detector response function model for multilayer small-diameter PET scanners," Phys. Med. Biol. **48**(8), 979–994 (2003).
[79]A. Rahmim, J. Tang, M. A. Lodge, S. Lashkari, M. R. Ay, R. Lautamaki, B. M. Tsui, and F. M. Bengel, "Analytic system matrix resolution modeling in PET: An application to Rb-82 cardiac imaging," Phys. Med. Biol. **53**(21), 5947–5965 (2008).
[80]R. H. Huesman, G. J. Klein, W. W. Moses, Q. Jinyi, B. W. Reutter, and P. R. G. Virador, "List-mode maximum-likelihood reconstruction applied to positron emission mammography (PEM) with irregular sampling," IEEE Trans. Med. Imaging **19**(5), 532–537 (2000).
[81]S. Moehrs, M. Defrise, N. Belcari, A. Del Guerra, A. Bartoli, S. Fabbri, and G. Zanetti, "Multi-ray-based system matrix generation for 3D PET reconstruction," Phys. Med. Biol. **53**(23), 6925–6945 (2008).
[82]E. U. Mumcuoglu, R. M. Leahy, S. R. Cherry, and E. Hoffman, "Accurate geometric and physical response modelling for statistical image reconstruction in high resolution PET," in *Conference Record IEEE Nuclear Science Symposium* (1996), pp. 1569–1573.
[83]M. Defrise, P. E. Kinahan, D. W. Townsend, C. Michel, M. Sibomana, and D. F. Newport, "Exact and approximate rebinning algorithms for 3-D PET data," IEEE Trans. Med. Imaging **16**(2), 145–158 (1997).
[84]L. Le Meunier, P. J. Slomka, D. Dey, A. Ramesh, L. E. J. Thomson, S. W. Hayes, J. D. Friedman, V. Cheng, G. Germano, and D. S. Berman, "Enhanced definition PET for cardiac imaging," J. Nucl. Cardiol. **17**(3), 414–426 (2010).
[85]L. Le Meunier, P. J. Slomka, D. Dey, A. Ramesh, L. E. J. Thomson, S. W. Hayes, J. D. Friedman, V. Cheng, G. Germano, and D. S. Berman, "Motion frozen F-18-FDG cardiac PET," J. Nucl. Cardiol. **18**(2), 259–266 (2011).
[86]T. Frese, N. C. Rouze, C. A. Bouman, K. Sauer, and G. D. Hutchins, "Quantitative comparison of FBP, EM, and Bayesian reconstruction algorithms for the IndyPET scanner," IEEE Trans. Med. Imaging **22**(2), 258–276 (2003).
[87]K. Lee, P. E. Kinahan, J. A. Fessler, R. S. Miyaoka, M. Janes, and T. K. Lewellen, "Pragmatic fully 3D image reconstruction for the MiCES mouse imaging PET scanner," Phys. Med. Biol. **49**(19), 4563–4578 (2004).
[88]J. Zhou and J. Qi, "Fast and efficient fully 3D PET image reconstruction using sparse system matrix factorization with GPU acceleration," Phys. Med. Biol. **56**(20), 6739–6757 (2011).
[89]A. Ruangma, B. Bai, J. S. Lewis, X. Sun, M. J. Welch, R. Leahy, and R. Laforest, "Three-dimensional maximum a posteriori (MAP) imaging with radiopharmaceuticals labeled with three Cu radionuclides," Nucl. Med. Biol. **33**(2), 217–226 (2006).
[90]A. F. Bielajew and D. W. O. Rogers, "Presta—The parameter reduced electron-step transport algorithm for electron Monte-Carlo transport," Nucl. Instrum. Methods B **18**(2), 165–181 (1987).
[91]M. R. Palmer and G. L. Brownell, "Annihilation density distribution calculations for medically important positron emitters," IEEE Trans. Med. Imaging **11**(3), 373–378 (1992).
[92]S. E. Derenzo, "Mathematical Removal of Positron Range Blurring in High Resolution Tomography," IEEE Trans. Nucl. Sci. **33**(1), 565–569 (1986).
[93]M. R. Palmer, Z. Xuping, and J. A. Parker, "Modeling and simulation of positron range effects for high resolution PET imaging," IEEE Trans. Nucl. Sci. **52**(5), 1391–1395 (2005).
[94]R. L. Harrison, M. S. Kaplan, S. D. Vannoy, and T. K. Lewellen, "Positron range and coincidence non-collinearity in SimSET," IEEE Nucl. Sci. Conf. Rec. 1265–1268 (1999).
[95]C. S. Levin and E. J. Hoffman, "Calculation of positron range and its effect on the fundamental limit of positron emission tomography system spatial resolution," Phys. Med. Biol. **44**(3), 781–799 (1999).
[96]B. Bai, A. Ruangma, R. Laforest, Y. C. Tai, and R. M. Leahy, "Positron range modeling for statistical PET image reconstruction," in *Nuclear Science Symposium Conference Record, 2003* (IEEE, 2003), Vol. 2504, pp. 2501–2505.

[97]A. Rahmim, J. Tang, M. A. Lodge, S. Lashkari, M. R. Ay, and F. M. Bengel, "Resolution modeled PET image reconstruction incorporating space-variance of positron range: Rubidium-82 cardiac PET imaging," IEEE Nucl. Sci. Symp. Conf. Rec. 3643–3650 (2008).
[98]A. Alessio and L. MacDonald, "Spatially variant positron range modeling derived from CT for PET image reconstruction," in *IEEE NSS/MIC Conference Proceedings*, 2008.
[99]L. Katz and A. S. Penfold, "Range-energy relations for electrons and the determination of beta-ray end-point energies by absorption," Rev. Mod. Phys. **24**(1), 28–44 (1952).
[100]L. Fu and J. Qi, "A residual correction method for high-resolution PET reconstruction with application to on-the-fly Monte Carlo based model of positron range," Med. Phys. **37**(2), 704–713 (2010).
[101]B. Bai, R. Laforest, A. M. Smith, and R. M. Leahy, "Evaluation of MAP image reconstruction with positron range modeling for 3D PET," in *Nuclear Science Symposium Conference Record, 2005* (IEEE, 2005), pp. 2686–2689.
[102]A. Tahari, P. E. Bravo, A. Rahmim, F. M. Bengel, and Z. Szabo, "Initial human experience with Rubidium-82 Renal PET/CT Imaging," Journal of Medical Imaging and Radiation Oncology (accepted for publication) (2013).
[103]A. Rahmim, J.-C. Cheng, and V. Sossi, "Improved noise propagation in statistical image reconstruction with resolution modeling," in *Nuclear Science Symposium Conference Record, 2005* (IEEE, 2005), pp. 2576–2578.
[104]J. Qi, "A unified noise analysis for iterative image estimation," Phys. Med. Biol. **48**, 3505–3519 (2003).
[105]S. Tong, A. M. Alessio, and P. E. Kinahan, "Noise and signal properties in PSF-based fully 3D PET image reconstruction: An experimental evaluation," Phys. Med. Biol. **55**(5), 1453–1473 (2010).
[106]S. A. Blinder, K. Dinelle, and V. Sossi, "Scanning rats on the high resolution research tomograph (HRRT): A comparison study with a dedicated micro-PET," Med. Phys. **39**(8), 5073–5083 (2012).
[107]T.-S. Lee, R. Lautamaki, T. Higuchi, F. Bengel, and B. M. W. Tsui, "Task-based human observer study for evaluation and optimization of 3D & 4D image reconstruction methods for gated myocardial perfusion SPECT," J. Nucl. Med. **50**(Suppl. 2), 524 (2009).
[108]T.-S. Lee, F. Bengel, and B. M. W. Tsui, "Task-based human observer study for evaluation of 4D MAP-RBI-EM method for gated myocardial perfusion SPECT," J. Nucl. Med. **49**(Suppl. 1), 153P (2008).
[109]R. F. Wagner and D. G. Brown, "Unified SNR analysis of medical imaging-systems," Phys. Med. Biol. **30**(6), 489–518 (1985).
[110]D. W. Wilson, Ph.D. dissertation, University of North Carolina at Chapel Hill, 1994.
[111]E. C. Frey and B. M. W. Tsui, *Collimator-Detector Response Compensation in SPECT* (Springer Science + Business Media, Inc., New York, NY, 2006).
[112]D. J. Kadrmas, M. E. Casey, N. F. Black, J. J. Hamill, V. Y. Panin, and M. Conti, "Experimental comparison of lesion detectability for four fully-3D PET reconstruction schemes," IEEE Trans. Med. Imaging **28**(4), 523–534 (2009).
[113]D. J. Kadrmas, M. E. Casey, M. Conti, B. W. Jakoby, C. Lois, and D. W. Townsend, "Impact of time-of-flight on PET tumor detection," J. Nucl. Med. **50**(8), 1315–1323 (2009).
[114]H. C. Gifford, P. E. Kinahan, C. Lartizien, and M. A. King, "Evaluation of multiclass model observers in PET LROC studies," IEEE Trans. Nucl. Sci. **54**(1), 116–123 (2007).
[115]J. Schaefferkoetter, M. Casey, D. Townsend, and G. El Fakhri, "Clinical impact of time-of-flight and point response modeling in PET reconstructions: a lesion detection study," Phys. Med. Biol. **58**, 1465–1478 (2013).
[116]G. Akamatsu, K. Ishikawa, K. Mitsumoto, T. Taniguchi, N. Ohya, S. Baba, K. Abe, and M. Sasaki, "Improvement in PET/CT image quality with a combination of point-spread function and time-of-flight in relation to reconstruction parameters," J. Nucl. Med. **53**(11), 1716–1722 (2012).
[117]B. Bai and P. D. Esser, "The effect of edge artifacts on quantification of positron emission tomography," in *Nuclear Science Symposium Conference Record (NSS/MIC), 2010* (IEEE, 2010), pp. 2263–2266.
[118]D. L. Snyder, M. I. Miller, L. J. Thomas, and D. G. Politte, "Noise and edge artifacts in maximum-likelihood reconstruction for emission tomography," IEEE Trans. Med. Imaging **MI-6**, 228–238 (1987).
[119]S. Tong, A. M. Alessio, K. Thielemans, C. Stearns, S. Ross, and P. E. Kinahan, "Properties and mitigation of edge artifacts in PSF-based PET reconstruction," IEEE Trans. Nucl. Sci. **58**(5), 2264–2275 (2011).
[120]D. G. Politte and D. L. Snyder, "The use of constraints to eliminate artifacts in maximum-likelihood image estimation for emission tomography," IEEE Trans. Nucl. Sci. **35**(1), 608–610 (1988).
[121]D. L. Snyder and M. I. Miller, "The use of sieves to stabilize images produced with the EM algorithm for emission tomography," IEEE Trans. Nucl. Sci. **32**(5), 3864–3872 (1985).
[122]C. C. Watson, "Estimating effective model kernel widths for PSF reconstruction in PET," in *2011 IEEE Nuclear Science Symposium and Medical Imaging Conference (Nss/Mic)* (2011), pp. 2368–2374.
[123]R. B. Innis, V. J. Cunningham, J. Delforge, M. Fujita, A. Gjedde, R. N. Gunn, J. Holden, S. Houle, S. C. Huang, M. Ichise, H. Iida, H. Ito, Y. Kimura, R. A. Koeppe, G. M. Knudsen, J. Knuuti, A. A. Lammertsma, M. Laruelle, J. Logan, R. P. Maguire, M. A. Mintun, E. D. Morris, R. Parsey, J. C. Price, M. Slifstein, V. Sossi, T. Suhara, J. R. Votaw, D. F. Wong, and R. E. Carson, "Consensus nomenclature for in vivo imaging of reversibly binding radioligands," J. Cereb. Blood Flow Metab. **27**(9), 1533–1539 (2007).
[124]J. S. Kim, J. S. Lee, K. C. Im, S. J. Kim, S. Y. Kim, D. S. Lee, and D. H. Moon, "Performance measurement of the microPET focus 120 scanner," J. Nucl. Med. **48**(9), 1527–1535 (2007).
[125]L. W. Locke, S. S. Berr, and B. K. Kundu, "Image-derived input function from cardiac gated maximum a posteriori reconstructed PET images in mice," Mol. Imaging Biol. **13**(2), 342–347 (2011).
[126]A. Pecking, D. Bellet, and J. Alberini, "Immuno-SPET/CT and immuno-PET/CT: A step ahead to translational imaging," Clin. Exp. Metastasis **29**, 847–852 (2012).
[127]A. Rahmim and J. Tang, "Impact of resolution modeling on detectability: analysis in terms of noise-equivalent quanta," *Proceedings of the Society of Nuclear Medicine & Molecular Imaging Annual Meeting*, Vancouver, June 8–12, 2013.